Improvement and error analysis of quantitative information extraction in diffraction-enhanced imaging*

Yang Hao(杨 浩), Xuan Rui-Jiao(轩瑞娇), Hu Chun-Hong(胡春红)†, and Duan Jing-Hao(段敬豪)

College of Biomedical Engineering, Tianjin Medical University, Tianjin 300070, *China*

(Received 21 May 2013; revised manuscript received 24 August 2013; published online 10 February 2014)

Diffraction-enhanced imaging (DEI) is a powerful phase-sensitive technique that provides higher spatial resolution and supercontrast of weakly absorbing objects than conventional radiography. It derives contrast from the X-ray absorption, refraction, and ultra-small-angle X-ray scattering (USAXS) properties of an object. The separation of different-contrast contributions from images is an important issue for the potential application of DEI. In this paper, an improved DEI (IDEI) method is proposed based on the Gaussian curve fitting of the rocking curve (RC). Utilizing only three input images, the IDEI method can accurately separate the absorption, refraction, and USAXS contrasts produced by the object. The IDEI method can therefore be viewed as an improvement to the extended DEI (EDEI) method. In contrast, the IDEI method can circumvent the limitations of the EDEI method well since it does not impose a Taylor approximation on the RC. Additionally, analysis of the IDEI model errors is performed to further investigate the factors that lead to the image artifacts, and finally validation studies are conducted using computer simulation and synchrotron experimental data.

Keywords: X-ray imaging, phase contrast, phase retrieval, synchrotron radiation

PACS: 87.59.–e, 87.64.mh, 42.30.Rx, 41.60.Ap **DOI:** 10.1088/1674-1056/23/4/048701

1. Introduction

Conventional radiography is an invaluable tool in medical, biological, and material fields, and derives contrast from the differences in the X-ray absorption between tissues. However, conventional radiography cannot clearly reveal the structural details of weakly absorbing objects that have identical or similar absorption characteristics. X-ray phase-contrast imaging (PCI) is a new imaging technique that exploits a contrast mechanism based on differences in the X-ray refractive index distribution of an object,[1–7] and it mainly derives contrast from the phase modulations induced by the object onto the transmitted X-ray beam. In fact, the behavior of X-rays while traversing an object can be described by the complex refractive index $n = 1 - \delta - \mathrm{i}\beta$. The real part δ incorporates the refractive effects and results in a phase shift (namely phase modulation), while the imaginary part β describes the absorption. In X-ray regions, the phase shift is more than 1000 times larger than the absorption term.[1] This implies that the PCI technique may provide much higher sensitivity than conventional radiography, especially for weakly absorbing objects where the absorption differences are very small.

While an X-ray beam transmits through a sample, the interactions between the X-ray and the sample are very complex, involving absorption, refraction, ultra-small-angle X-ray scattering (USAXS), etc. As one of many effective PCI techniques, diffraction-enhanced imaging (DEI) can generate contrast from the X-ray absorption, refraction, and USAXS properties of an object.[8,9] Moreover, DEI utilizes an analyzer crystal with high angular sensitivity to measure the three contrasts of the object, which dramatically improves the contrast and spatial resolution of the images. The three contrast mechanisms can be utilized to provide three parametric images that depict, respectively, the physical properties of absorption, refraction, and USAXS produced by the object. In practice, extracting quantitative X-ray absorption, refraction, and USAXS information from the images is critical to the research and application of DEI. In order to both effectively extract the different physical properties and accurately quantify them, several mathematical methods have been proposed so far.[10–21] The independent object properties may play a useful role in identifying the structures and features in the object. In recent years, different information extraction methods, based on the geometrical optics (GO) approximation, have been widely used to extract quantitative information from the DEI images in biological, material, and medical fields.[22–28]

In this paper, the improved DEI (IDEI) method, which is based on Gaussian curve fitting of the rocking curve (RC), is proposed after comprehensive comparison with typical GO extraction methods in terms of the imaging time and the accuracy of the extracted information. The objectives of this paper are to demonstrate the validity of the IDEI method in extracting quantitative information when time and dose constraints are relevant. The method is validated by making use of computer-simulated and experimental synchrotron data.

*Project supported by the National Natural Science Foundation of China (Grant Nos. 30900333 and 81371549) and the WBE Liver Fibrosis Foundation, China (Grant No. CFHPC20131033).

†Corresponding author. E-mail: chunhong_hu@hotmail.com

© 2014 Chinese Physical Society and IOP Publishing Ltd

2. The principle of DEI

A typical schematic of the DEI setup is illustrated in Fig. 1(a). The DEI setup consists of a monochromator crystal, an analyzer crystal, a sample stage between them, and an X-ray CCD detector. The monochromator crystal is used to select the energy range of the X-ray from the incident synchrotron beam and to generate an almost monochromatic X-ray beam. Then, the monochromatic beam transmitted through the sample is incident on the analyzer crystal, and the intensity of the X-ray beam reflected by the analyzer crystal is measured by a detector.[8] Obviously, a matched monochromator-analyzer crystal system is introduced in DEI, and the behavior of the X-rays prepared by the monochromator crystal after passing through an object is determined by the analyzer. The analyzer acts as an angular filter of the radiation transmitted through the object, and can modulate the beam by converting a small X-ray propagation angular change to a variation in the intensity onto the detector. The angular acceptance or reflectivity of the analyzer crystal is characterized by its RC, as shown in Fig. 1(b). The full width at half maximum (FWHM) of the RC is typically on the order of a few microradians, which is approximately equal to the Darwin width (w_D) of the crystal, so the analyzer crystal has a high angular sensitivity. In DEI, varying image contrast can be obtained at different angular positions along the RC. In particular, the meaningful positions are at the peak or the slope of its RC. At the peak position of the RC, the analyzer crystal is exactly parallel to the monochromator, and the peak image highlights the so-called extinction contrast caused by the scattering rejection. At the slope position of the RC, refraction causes an intensity change. Moreover, the RC slope acts as a contrast amplifier. The image intensity variation due to refraction effects becomes greater when the slope is steeper.[8]

As discussed above, DEI provides a way of imaging various contrast mechanisms from an object's X-ray absorption, refraction, and USAXS properties, and the DEI image thus contains information about absorption, refraction, and USAXS. The information in the image is very rich, but it can lead to ambiguous image interpretation due to the superposition between signals. Independent information about absorption, refraction, and USAXS can be extracted by combining two or more images acquired at different positions on the RC, and these are used to present the absorption, refraction, and USAXS images, namely the parametric images. In fact, the various contrast mechanisms have their own characteristics, and they can provide information about the tissue structures on different scales. The absorption contrast is generated by the variations in the X-ray absorption coefficient within the object. The refraction contrast highlights the tissue contours within the object, and this is more sensitive to density variations of the weakly absorbing objects than the absorption contrast. The USAXS contrast is caused by the presence of textural structure within the object on a scale smaller than a pixel, and it may differentiate homogeneous tissues from tissues that are irregular on a scale of micrometers,[22] which provides a powerful tool to distinguish between pathologic lesions and normal tissues. The refraction and USAXS contrast mechanisms are ideally suited to weakly absorbing object imaging because of the improved sensitivity.

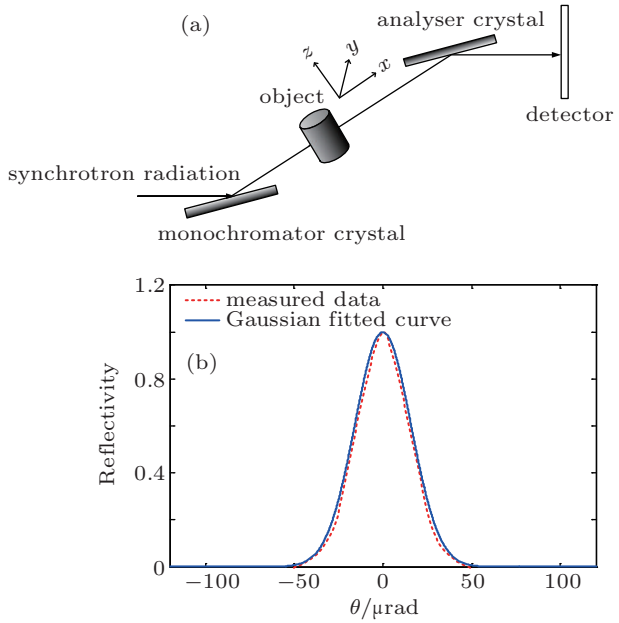


Fig. 1. (color online) Schematic diagram of the DEI setup (a) and the RC (b) of the DEI system in the experiment. The measured (dashed line) RC and fitted (solid line) RC are shown in panel (b), respectively, and the RC corresponds to a silicon 111 (Si 111) reflection at 10 keV.

3. The quantitative information extraction method of the DEI images

The classic DEI method was introduced by Chapman *et al.* in 1997.[8] The DEI method enables the separation of the absorption and refraction images by using only two half-slope images based on a first-order Taylor approximation of the RC. The simple calculation model facilitates the application of the DEI method in practice, which enables it to achieve widespread applications in medical, biological, and material fields. However, the DEI method has several intrinsic shortcomings. Most of all, it does not take account of the USAXS produced by the object. Actually, the effect of USAXS is not negligible for biological tissues, and thus the absorption and refraction images may produce highly erroneous results when imaging biological tissues. Moreover, USAXS is an important contrast mechanism that can convey the presence of microstructures in the object. In order to overcome the limitations of the DEI method, some mathematical methods have been proposed to separate the contrasts from absorption, refraction, and USAXS by combining three or more of the images acquired at different positions on the RC. Obvi-

ously, the methods requiring few images have obvious advantages when considering time and dose constraints. In recent years, an extended DEI (EDEI) method was proposed based on a second-order Taylor approximation of the RC.[14,15] The EDEI method utilizes only three images to produce the parametric images that depict an object's projected X-ray absorption, refraction, and USAXS properties. When the analyzer is set to be at a given position θ on the RC, the EDEI imaging model can be expressed as

$$\begin{aligned} & g(\theta;x,y) \\ &= I_{\mathrm{R}}(x,y)\left\{R(\theta)+\left.\frac{\mathrm{d}R}{\mathrm{d}\theta}\right|_{\theta}\Delta\theta\,(x,y)+\frac{1}{2}\left.\frac{\mathrm{d}^2R}{\mathrm{d}\theta^2}\right|_{\theta}\right. \\ &\quad\times\left.\left[\sigma_{\mathrm{s}}^2\,(x,y)+(\Delta\theta\,(x,y))^2\right]\right\}, \end{aligned} \tag{1}$$

where $g(\theta;x,y)$ is the intensity reaching the detector, $I_{\mathrm{R}}(x,y)$ is the apparent absorption intensity, $R(\theta)$ denotes the intrinsic rocking curve, $\Delta\theta\,(x,y)$ describes the refraction angle, and $\sigma_{\mathrm{s}}^2\,(x,y)$ denotes the standard deviation of the scattering distribution, namely the USAXS image. Equation (1) establishes a nonlinear relationship between the intensity data $g(\theta;x,y)$ and the absorption, refraction, and USAXS properties of the object. Obviously, the parametric images can be analytically calculated if the DEI images are acquired at three distinct analyzer angular positions. However, a second-order Taylor expansion to the analyzer RC is only a good approximation for small angular deviations, and this method will lead to imprecise results when the refractive and/or scattering deviations are larger than the FWHM of the RC.

To overcome the limitations of the DEI method, multiple image radiography (MIR) was also proposed in 2003.[10–13] MIR has a significant improvement over DEI based on statistical analysis, and it can produce true absorption, refraction, and USAXS images. As described in MIR, the effect of the object on the beam is regarded as a linear system in terms of the angle θ. It has been demonstrated that the intensity data function $g(\theta;x,y)$ can be expressed as

$$\begin{aligned} g\,(\theta;x,y) &= \int_{-\infty}^{+\infty} f\left(\theta';x,y\right)R\left(\theta-\theta'\right)\mathrm{d}\theta' \\ &= R\,(\theta)*f\,(\theta;x,y)\,, \end{aligned} \tag{2}$$

where $f(\theta;x,y)$ represents the angular response function of the object and characterizes the object. Physically, $f(\theta;x,y)$ represents the angular intensity spectrum of the transmitted beam that would result from illuminating the object with a perfectly collimated incident beam. Obviously, $f(\theta;x,y)$ is the kernel of Eq. (2), and can be used to estimate the parametric images. By introducing a probabilistic interpretation, $f(\theta;x,y)$ can be described as[14,15]

$$f\,(\theta;x,y)=I_{\mathrm{R}}\,(x,y)\,P\,(\theta;x,y)\,, \tag{3}$$

where the probability density function $P\,(\theta;x,y)$ describes the angular distribution of photons participating in USAXS or refraction at location (x,y) in the object plane, and its expression is given by

$$P\,(\theta;x,y)=\frac{1}{\sigma_{\mathrm{s}}\,(x,y)\,\sqrt{2\pi}}\exp\left(\frac{-\left(\theta-\Delta\theta\,(x,y)\right)^2}{2\sigma_{\mathrm{s}}^2\,(x,y)}\right). \tag{4}$$

In Eq. (2), the intrinsic rocking curve $R(\theta)$ is a known description of the imaging system. Actually, $R(\theta)$ can be well fitted by a Gaussian curve, and is expressed as

$$R(\theta)=A_0\exp\left(\frac{-\theta^2}{2\sigma^2}\right), \tag{5}$$

where $w_{\mathrm{D}}=2\sigma\,(2\ln 2)^{1/2}$ and A_0 is the area of the RC. By making use of Eqs. (2)–(5), $g(\theta;x,y)$ can be given by

$$g\,(\theta;x,y)=\frac{A_0\sigma I_{\mathrm{R}}(x,y)}{\sqrt{\sigma_{\mathrm{s}}^2(x,y)+\sigma^2}}\exp\left(\frac{-\left(\theta-\Delta\theta(x,y)\right)^2}{2\left(\sigma_s^2(x,y)+\sigma^2\right)}\right). \tag{6}$$

The IDEI method is proposed based on Eq. (6). Because the second-order Taylor expansion represents an inadequate approximation of the RC, the IDEI method exhibits significant advantages when compared with the EDEI method.

By making use of the logarithm, equation (6) can be expressed as

$$\ln\left[g\,(\theta;x,y)\right]=a\theta^2+b\theta+c, \tag{7}$$

where

$$\begin{cases} a=\dfrac{-1}{2(\sigma_{\mathrm{s}}^2(x,y)+\sigma^2)}, \\ b=\dfrac{\Delta\theta(x,y)}{(\sigma_{\mathrm{s}}^2(x,y)+\sigma^2)}, \\ c=-\dfrac{\Delta\theta^2(x,y)}{2(\sigma_{\mathrm{s}}^2(x,y)+\sigma^2)}+\ln(A_0\sigma I_{\mathrm{R}}(x,y)) \\ \quad\quad -\dfrac{1}{2}\ln(\sigma_{\mathrm{s}}^2(x,y)+\sigma^2). \end{cases} \tag{8}$$

By choosing three distinct analyzer crystal orientations, θ_1, θ_2, and θ_3, we can obtain

$$\begin{cases} \ln[g(\theta_1;x,y)]=a\theta_1^2+b\theta_1+c, \\ \ln[g(\theta_2;x,y)]=a\theta_2^2+b\theta_2+c, \\ \ln[g(\theta_3;x,y)]=a\theta_3^2+b\theta_3+c. \end{cases} \tag{9}$$

According to Eq. (8), the solution of Eq. (9) provides three parametric images, namely the apparent absorption image $I_{\mathrm{R}}(x,y)$, the refraction angle image $\Delta\theta\,(x,y)$, and the USAXS image $\sigma_{\mathrm{s}}^2\,(x,y)$. In general, the MIR method requires more than five images in quantitative information extraction, while the IDEI method needs only three. In contrast to the MIR method, IDEI significantly reduces possible radiation doses while circumventing the limitations of EDEI.

4. Analysis of IDEI model errors

In the IDEI model, it is very important to investigate the factors that give rise to quantitative information extraction errors. In this section, we will analyze the effect of such errors on the fidelity of the reconstructed parametric image. In the process of measurement and digitalization, the image data will inevitably generate a rounding error due to the limitation of the sensitivity of the CCD device. Assuming that the bit depth of the measured image is n and that $g_{\max}$ is used to represent the maximum intensity detected by the detector, then the detected intensity of the X-ray is divided into 2^n parts, so the accurate extent of the measured data will be $g_{\max}/2^n$. The rounding error corresponds to the following formula:

$$|\varepsilon| \leq g_{\max}/2^{n+1}. \tag{10}$$

Actually, the measured intensity $g_0(\theta;x,y)$ is given by

$$g_0(\theta;x,y) = g(\theta;x,y) + \varepsilon, \tag{11}$$

where $g(\theta;x,y)$ is the theoretical intensity of the X-ray beam transmitted through the sample. By making use of the logarithm, equation (11) can be expressed as

$$\ln[g(\theta;x,y)] = \ln[g_0(\theta;x,y)] - \ln\left(1 + \frac{\varepsilon}{g(\theta;x,y)}\right), \tag{12}$$

where the rounding error ε is very small, and thus a simplified formula of Eq. (12) is given by

$$\ln[g(\theta;x,y)] \approx \ln[g_0(\theta;x,y)] - \frac{\varepsilon}{g(\theta;x,y)}. \tag{13}$$

It is obvious that an error $\varepsilon/g(\theta;x,y)$ will be introduced when solving Eq. (9). Now we define

$$\boldsymbol{A} = \begin{bmatrix} \theta_1^2 & \theta_1 & 1 \\ \theta_2^2 & \theta_2 & 1 \\ \theta_3^2 & \theta_3 & 1 \end{bmatrix}, \quad \boldsymbol{x} = \begin{bmatrix} a \\ b \\ c \end{bmatrix},$$

$$\boldsymbol{G} = \begin{bmatrix} \ln[g_0(\theta_1;x,y)] \\ \ln[g_0(\theta_2;x,y)] \\ \ln[g_0(\theta_3;x,y)] \end{bmatrix}, \quad \boldsymbol{E} = \begin{bmatrix} \dfrac{\varepsilon}{g(\theta_1;x,y)} \\ \dfrac{\varepsilon}{g(\theta_2;x,y)} \\ \dfrac{\varepsilon}{g(\theta_3;x,y)} \end{bmatrix}.$$

According to Eqs. (9) and (13), we can obtain the following equation:

$$\boldsymbol{A}\boldsymbol{x} = \boldsymbol{G} - \boldsymbol{E}. \tag{14}$$

In the solution of Eq. (14), the relative error is given by

$$\frac{\|\delta \boldsymbol{x}\|}{\|\boldsymbol{x}\|} \leq \mathrm{cond}(\boldsymbol{A}) \times \frac{\|\boldsymbol{E}\|}{\|\boldsymbol{G}\|}, \tag{15}$$

where $\|\bullet\|$ represents the L1-norm, and $\mathrm{cond}(\boldsymbol{A})$ is the condition number of matrix $\boldsymbol{A}$. Equation (15) shows that the relative error correlates with the values of $\mathrm{cond}(\boldsymbol{A})$ and $\|\boldsymbol{E}\|/\|\boldsymbol{G}\|$. For matrix $\boldsymbol{A}$ in Eq. (14), the condition number is determined by the chosen analyzer crystal orientations θ_1, θ_2, and θ_3. Thus, the choice of the analyzer crystal orientations plays an important role in accurately solving the equations. In practice, the quantitative information can be extracted reliably when the analyzer crystal orientations are acquired at the peak and the two middle slopes of $R(\theta)$, respectively.[14,15,19] Similarly, the magnitude of $\|\boldsymbol{G}\|$ is also relevant to the analyzer orientations θ_1, θ_2, and θ_3. In contrast, the effect of $\|\boldsymbol{E}\|$ on the relative error is the most complicated, and $\|\boldsymbol{E}\|$ is shown as follows:

$$\|\boldsymbol{E}\| = \left|\frac{\varepsilon}{g(\theta_1;x,y)}\right| + \left|\frac{\varepsilon}{g(\theta_2;x,y)}\right| + \left|\frac{\varepsilon}{g(\theta_3;x,y)}\right|. \tag{16}$$

Then,

$$\|\boldsymbol{E}\| \leq \left|\frac{3\varepsilon}{g(\theta_0;x,y)}\right|, \tag{17}$$

where

$$\begin{aligned} g(\theta_0;x,y) = {} & \min(g(\theta_1;x,y), g(\theta_2;x,y), g(\theta_3;x,y)) \\ & \times (\theta_0 \in (\theta_1, \theta_2, \theta_3)). \end{aligned} \tag{18}$$

In DEI, the maximum intensity reaching the detector is given by

$$g_{\max} = I_0 \times R(\theta_{\mathrm{B}}). \tag{19}$$

In Eq. (19), θ_{B} is the Bragg angle, where the intensity of the reflected X-ray reaches its maximum. According to Eq. (5), equation (19) can be expressed as

$$g_{\max} = I_0 \times A_0. \tag{20}$$

Additionally, $I_{\mathrm{R}}(x,y)$ is computed approximately as

$$I_{\mathrm{R}}(x,y) = I_0 \exp\left(-2k \int_{\mathrm{L}} \beta(x,y,z)\mathrm{d}z\right), \tag{21}$$

where k is the wave number and β corresponds to the attenuation coefficient of the object.

Combining Eqs. (6), (10), (17), (20), and (21), the range of $\|\boldsymbol{E}\|$ can be calculated by

$$\|\boldsymbol{E}\| \leq \frac{1}{\left|\dfrac{2^{(n+1)}}{3} \times \dfrac{C_\beta \sigma}{\sqrt{\sigma_{\mathrm{s}}^2(x,y) + \sigma^2}} \exp\left(\dfrac{-(\theta_0 - \Delta\theta(x,y))^2}{2(\sigma_{\mathrm{s}}^2(x,y) + \sigma^2)}\right)\right|}, \tag{22}$$

where $C_\beta = \exp(-2k\int_{\mathrm{L}} \beta(x,y,z)\mathrm{d}z)$.

For a quantitative analysis, $\min(1/\|\boldsymbol{E}\|)$ can be interpreted as the accuracy of the extracted information as a function of the simulated $\Delta\theta(x,y)$, and can be described by the Gaussian curve as shown in Fig. 2.

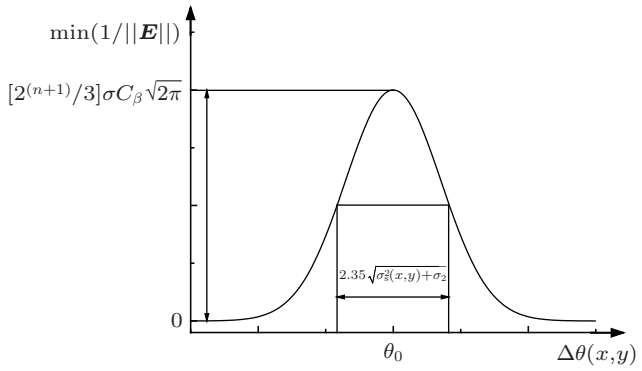


Fig. 2. Error analyses of the reconstructed images at each pixel for the different values of refraction angle $\Delta\theta(x,y)$. The FWHM of the Gaussian curve is $2.35\sqrt{\sigma_s^2(x,y)+\sigma^2}$ and the corresponding peak is $2^{(n+1)}\sigma C_\beta\sqrt{2\pi}/3$.

From Fig. 2, we can obtain the following points.

(i) The error increases with the increase in the deviation between θ_0 and $\Delta\theta(x,y)$. Consequently, a considerable quantitative information extraction error may be introduced at the edge of the object where refraction angle is larger.

(ii) The FWHM of the Gaussian curve is the following $2.35\sqrt{\sigma_s^2(x,y)+\sigma^2}$, which indicates that the width of the Gaussian curve will increase in the presence of USAXS. The introduction of USAXS not only enables the increase in the obtained range of $\Delta\theta(x,y)$ when the maximum error is constant, but can also reduce the quantitative information extraction error.

(iii) The peak value of the Gaussian curve is as follows: $2^{(n+1)}\sigma C_\beta\sqrt{2\pi}/3$. Obviously, the error will exponentially decrease with the increase in the image bit depth n. In other words, an increase of the image bit depth can significantly reduce the quantitative information extraction error.

5. Results

In this section, the developed GDEI method is investigated using computer-simulated results and experimental measurements.

5.1. Computer-simulated studies

We refer to the mathematical phantom shown in Fig. 3 according to the model proposed by Chou *et al.*,[15] which exhibits various combinations of refraction, absorption, and scattering effects. The phantom consists of a uniform Lucite rod (with radius 3 mm and length 7 mm) and different layers of paper. The Lucite rod, which serves as an absorptive–refractive object, is placed in front of the layers of paper. The paper is composed of fibrous structures and represents a scattering object that is expected to introduce USAXS, but little refraction and absorption. In our phantom, different layers of paper are arranged so that the number of layers of paper range from one to seven (namely 1, 3, 5, and 7), as shown in Fig. 3. Each layer of paper, which is 8 mm wide and 1.6 mm high, is assumed to produce USAXS, which is described by a Gaussian PDF characterized by a variance $\sigma_0^2 = 5\times10^{-12}$ rad^2. Thus, the value of USAXS can be determined as follows:

$$\sigma_s^2(x,y) = N(x,y)\sigma_0^2, \tag{23}$$

where $N(x,y)$ is the number of scattering layers at position (x,y). The phantom, illuminated by the X-ray energy of 20 keV, is characterized by a complex-valued refractive index $n = 1-\delta-\mathrm{i}\beta$ ($\delta = 6.666\times10^{-7}$ and $\beta = 2.854\times10^{-10}$). Additionally, the theoretical value of $\Delta\theta(x,y)$ can be expressed as

$$\Delta\theta(x,y) \approx \int_L \frac{\partial\delta(x,y,z)}{\partial x}\mathrm{d}z, \tag{24}$$

where L denotes the path of the beam through the object. The value of $I_R(x,y)$ is calculated according to Eq. (21), and the wave number k is 1.61×10^7 mm^{-1}.

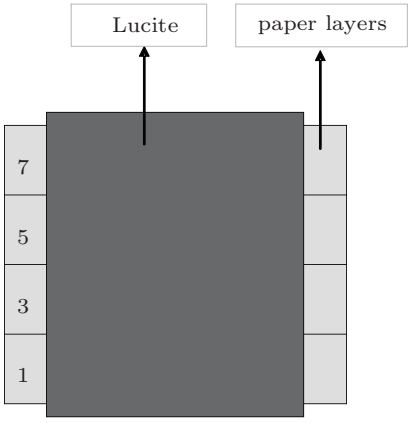


Fig. 3. Schematic diagram of the phantom used in the computer simulation. The phantom consists of a Lucite rod and different thickness sheets, and the arrangement of the paper introduces varying amounts of USAXS.

In this study, DEI images of the phantom can be acquired at different positions along the RC by means of Eq. (2), and the functions $R(\theta)$ and $f(\theta;x,y)$ are sampled in intervals of 0.1 μrad. The intensity detector contains 400 × 400 elements, each with the dimension 20 μm × 20 μm. Utilizing three input images, which are acquired at the peak and the two middle slopes of the RC, respectively, the IDEI and EDEI methods are utilized to separate the absorption, refraction, and USAXS information of the phantom.

Figure 4 shows the parametric images reconstructed using the EDEI method (top row), the 8-bit IDEI method (middle row), and the 16-bit IDEI method (bottom row). Note that the 8-bit and 16-bit IDEIs denote the IDEI methods that are based on 8-bit and 16-bit DEI images, respectively. As shown in Fig. 4(a), the absorption image reconstructed by the EDEI method contains artifacts that are pronounced in the upper-half of the image, where the USAXS is strongest. Moreover, the effect of the artifacts is reduced as the USAXS decreases. As a comparison, the artifacts do not emerge in the absorption images using the IDEI method (Figs. 4(d) and 4(g)), which

demonstrates the feasibility of pure absorption information extraction using the IDEI method. In addition, the comparison between Fig. 4(d) and Fig. 4(g) shows that the absorption image reconstructed using the 8-bit IDEI method is severely subjected to blocky artifacts. These artifacts derive from the rounding errors in the quantization process of the image, and can be perfectly solved by enhancing the bit depth of the image, as shown in Fig. 4(g).

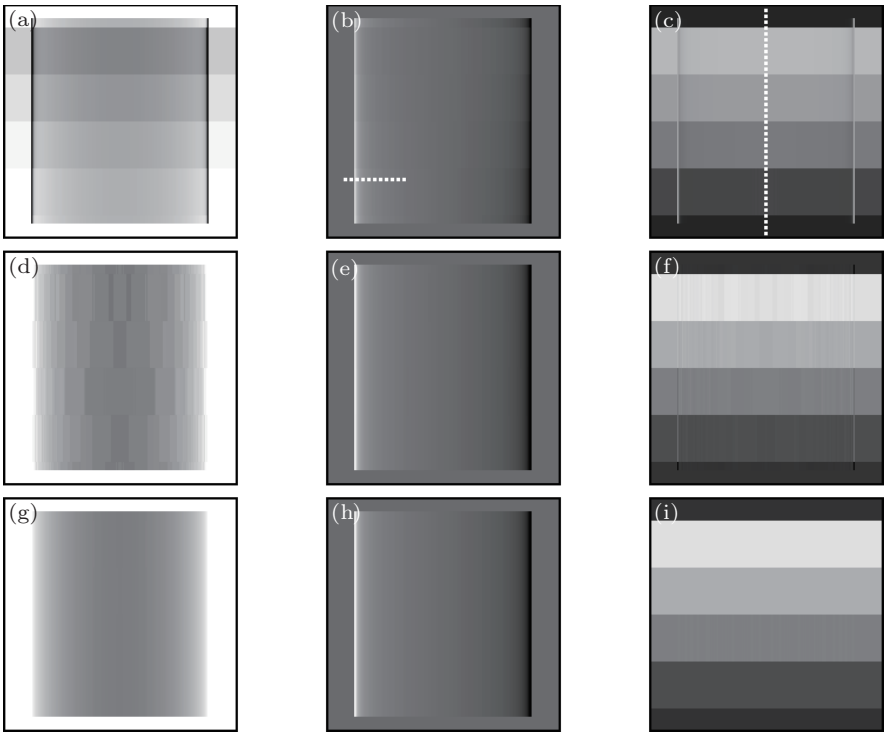


Fig. 4. Parametric images reconstructed from computer-simulated data. Panels (a)–(i) contain images that depict, respectively, the physical properties of absorption, refraction, and USAXS produced by the phantom. The absorption, refraction, and USAXS images are obtained by making use of the EDEI method (top row), the 8-bit IDEI method (middle row), and the 16-bit IDEI method (bottom row).

The quantitative analysis regarding the refraction images is revealed by the profiles in Fig. 5. The dashed line in Fig. 4(b) represents the profile position. Figure 5 contains the calculated profiles through Figs. 4(b), 4(e), and 4(h). These profiles are obtained using the EDEI, 8-bit IDEI and 16-bit IDEI methods. For comparison, the corresponding theoretical profile is also shown in Fig. 5. The image profiles confirm that all the methods show good agreement with the theory in regions where the refraction angles introduced by the rod are not very high. However, the difference between the methods is very pronounced at the Lucite rod boundary locations, where strong refraction occurs. At the edge of the Lucite rod, the calculated values from the 16-bit IDEI method are consistent with the theoretical values, the 8-bit IDEI method shows a discrepancy compared with the theoretical values, and the refraction angles are highly underestimated in the case of the EDEI method. As discussed above, a considerable quantitative information extraction error in the IDEI method may be introduced at the edge of the object, and the increase in the image bit depth can significantly reduce the corresponding error. For the EDEI method, the difference can be explained by the fact that the second-order Taylor approximation fails when the refraction angle is larger than the FWHM of the RC.

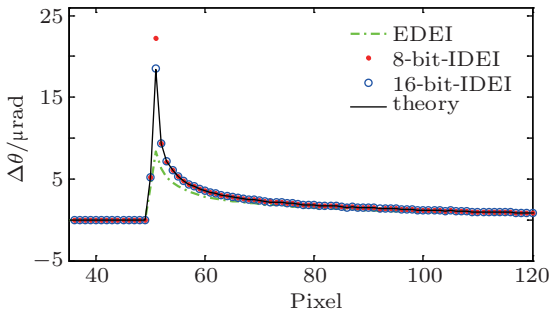


Fig. 5. (color online) The comparison among the refraction angle values extracted by the EDEI, 8-bit IDEI, and 16-bit IDEI methods. The profile position corresponds to the dashed line in Fig. 4(b). The values extracted by various methods are compared with the theoretical profile.

In order to study the effect of USAXS on the refraction information extraction, the calculated refraction angles at the right edge of the rod are presented in Table 1. As shown in Table 1, the refraction angles extracted with the 16-bit IDEI method accord with the theoretical values perfectly. However, the refraction angles extracted with the 8-bit IDEI method deviate from the theoretical value. Moreover, the deviation di-

minishes as the introduced value of USAXS increases because the introduction of USAXS can reduce the quantitative information extraction error, as discussed above. Due to the intrinsic limitations of the EDEI method, the calculated refraction angles are significantly lower than the theoretical values, and this phenomenon will be more evident with the increase in the value of USAXS.

Table 1. Comparisons among the refraction angles (in units of μrad) of the Lucite rod extracted by various methods with the increase in the value of USAXS.

Paper layers	Theory	EDEI	8-bit IDEI	16-bit IDEI
0	–16.298	–8.542	–14.257	–16.300
1	–16.298	–8.415	–17.545	–16.306
3	–16.298	–8.141	–15.803	–16.299
5	–16.298	–7.851	–16.621	–16.296
7	–16.298	–7.553	–15.983	–16.298

Figures 4(c), 4(f), and 4(i) show the USAXS images reconstructed using the EDEI, 8-bit IDEI, and 16-bit IDEI methods, respectively. All these methods are capable of producing clear USAXS images, and different scattering papers are visible and distinguishable after reconstruction. However, unlike the USAXS image produced by the 16-bit IDEI method, apparent linear artifacts are visible at the edge of the rod in the images (Figs. 4(c) and 4(f)), which represent a form of contamination from strong refraction. This shows that the 16-bit IDEI method can provide a USAXS image without contamination from the refraction and absorption effects compared with the EDEI and 8-bit IDEI methods. For a further quantitative analysis, figure 6 contains the vertical profiles through the USAXS images along the vertical line marked with dashed line in Fig. 4(c). The image profiles confirm that the 8-bit IDEI and 16-bit IDEI methods can produce accurate estimates of the reconstructed USAXS distribution compared with the EDEI method. The EDEI method can accord with the theoretical values well in the region corresponding to a single scattering layer, where the scattering is not strong. However, the values extracted using the EDEI method are underestimated as the number of scattering layers increases.

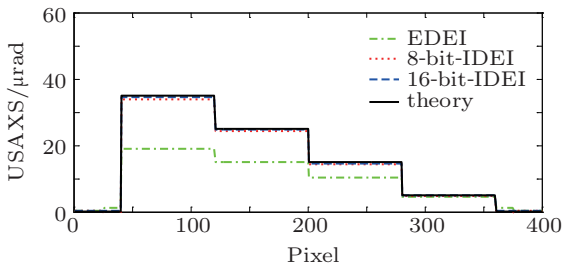


Fig. 6. (color online) The USAXS profiles from the vertical line across the images in Figs. 4(c), 4(f), and 4(i), and the profile position corresponding to the dashed line in Fig. 4(c). The results from the EDEI, 8-bit IDEI, and 16-bit IDEI methods are shown, and the corresponding theatrical values are also presented.

5.2. Experimental studies

The experiment was performed at the 4W1A beamline of the Beijing Synchrotron Radiation Facility (BSRF). Two perfect Si (111) crystals were used as the monochromator and analyzer. The tunable energy range of the X-ray beam was 3 keV–22 keV, and the X-ray beam energy in the experiments was set at 10 keV for the plastic cylinder sample. The plastic cylinder was cut from a common ballpoint pen refill. Its outer diameter was 3 mm and its inner diameter was 1.5 mm. In order to study the effect of USAXS on the information extraction, paper was introduced and placed behind the plastic cylinder. The X-ray source was a wiggler that emits radiation, and whose center was placed 43 m away from the experimental area. The detector employed an X-ray FDI-18-mm camera system (Photonic Science Ltd.) with 1300×1030 pixels, and 10.9 μm×10.9 μm per pixel. The detector system had a field of view of 20 mm ×10 mm, with a sample-to-detector distance of about 30 cm.

The absorption images of the plastic cylinder were reconstructed using the IDEI method. Figures 7(a) and 7(b) show the absorption images of the plastic cylinder without and with the introduction of paper, respectively. Obviously, the two images look very similar, and exhibit the expected absorption features of the sample. However, the apparent bright lines at the edge of the plastic cylinder are visible in Fig. 7(a), and are a contamination from strong refraction. According to Fig. 2, the introduction of paper may reduce the corresponding quantitative information extraction error, as shown in Fig. 7(b).

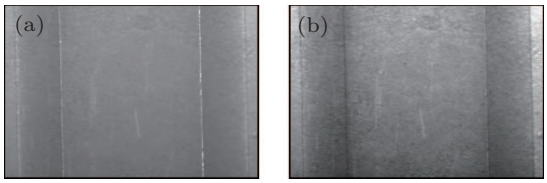


Fig. 7. The absorption images of the plastic cylinder reconstructed using the IDEI method without (a) and with (b) the introduction of paper, respectively.

By making use of the IDEI method, figures 8(a) and 8(c) show the reconstructed refraction images of the plastic cylinder without and with the introduction of paper, respectively. For comparison, the corresponding refraction images are presented in Figs. 8(b) and 8(d) using the EDEI method. Quantitative comparison between the reconstructed refraction images using the two methods is revealed by the profiles in Fig. 9. Figure 9 contains the calculated profiles from the four images in Fig. 8, and the dashed line in Fig. 8(a) represents the corresponding profile position. As shown in Fig. 9, the profiles show a basic consistency in regions where the refraction an-

gles introduced by the cylinder are small. However, the refraction angles are highly underestimated in the case of the EDEI method when the profiles appear at the edges of the cylinder. Moreover, the extracted refraction angles in Fig. 8(a) are consistent with those in Fig. 8(c), and the extracted refraction angles in Fig. 8(d) show obvious underestimation compared with those in Fig. 8(b). The results imply that the IDEI method allows better separation of the refractive information from USAXS.

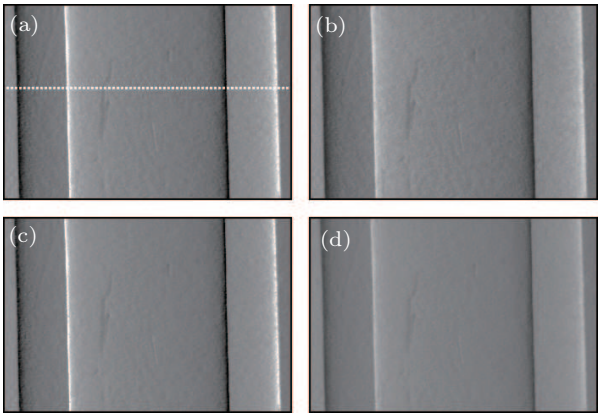


Fig. 8. Refraction images of the plastic cylinder reconstructed using the EDEI and IDEI methods, respectively.

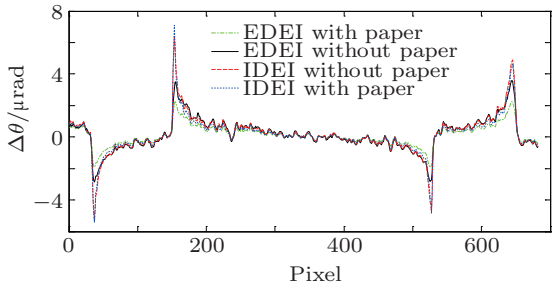


Fig. 9. (color online) The profiles of the refraction images shown in Fig. 8. The profile position corresponds to the dashed line in Fig. 8(a).

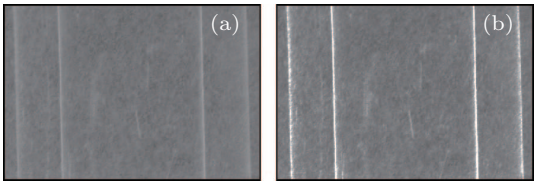


Fig. 10. USAXS images of the plastic cylinder with the introduction of paper. Panels (a) and (b) show the USAXS images obtained using the IDEI and EDEI methods, respectively.

A comparison between the USAXS images extracted using the IDEI and EDEI methods is shown in Fig. 10. The plastic cylinder with the introduction of paper is used to produce the USAXS image. Figures 10(a) and 10(b) show the reconstructed USAXS images using the IDEI and EDEI methods, respectively. Obviously, the IDEI method can extract the USAXS information and display the expected USAXS features of the sample better. In contrast, the apparent bright lines at the edge of the plastic cylinder are clearly visible in Fig. 10(b). As discussed before, this is a type of contamination from strong refraction.

6. Conclusions

Quantitative extraction of X-ray absorption, refraction, and USAXS information from the images is a key issue for potential application of DEI. In this paper, the IDEI method is proposed and investigated based on the previous EDEI method, and can produce parametric images that reveal the absorption, refractive, and USAXS properties of an object. The IDEI method does not impose a Taylor approximation on the analyzer RC, and thus it can circumvent the limitations of the EDEI method well. In practice, the accuracy obtained by the IDEI method is substantially higher than that achieved by the EDEI method. Compared with the MIR method, the IDEI method needs only three images, which is definitely an advantage in the reduction of the acquisition time and the dose delivered to the sample. Analysis of the IDEI model errors is performed to investigate the factors that give rise to quantitative information extraction errors. Explicit expressions are provided to analyze the effect of such errors on the fidelity of the reconstructed parametric images. Finally, the IDEI method and corresponding model errors are validated using computer-simulated and experimental data.

Acknowledgment

The authors would like to thank Prof. Zhu Pei-Ping, Dr. Yuan Qing-Xi, and Dr. Huang Wan-Xia from the Beijing Synchrotron Radiation Facility (BSRF) for their assistance in our experiments.

References

[1] Momose A, Takeda T, Itai Y and Hirano K 1996 *Nat. Med.* **2** 473
[2] Davis T J, Gao D, Gureyev T E, Stevenson A W and Wilkins S W 1995 *Nature* **373** 595
[3] Wilkins S W, Gureyev T E, Gao D, Pogany A and Stevenson A W 1996 *Nature* **384** 335
[4] Pfeiffer F, Weitkamp T, Bunk O and David C 2006 *Nat. Phys.* **2** 258
[5] Liu X S, Li E R, Zhu P P, Liu Y J, Zhang K, Wang Z L, Hong Y L, Zhang H T, Yuan Q X, Huang W X and Wu Z Y 2010 *Chin. Phys. B* **19** 040701
[6] Liu X, Guo J C and Niu H B 2010 *Chin. Phys. B* **19** 070701
[7] Lei Y H, Liu X, Guo J C, Zhao Z G and Niu H B 2011 *Chin. Phys. B* **20** 042901
[8] Chapman D, Thomlinson W, Johnston R E, Washburn D, Pisano E, Gmür N, Zhong Z, Menk R H, Arfelli F and Sayers D 1997 *Phys. Med. Biol.* **42** 2015
[9] Zhu P P, Yuan Q X, Huang W X, Wang Y, Shu H, Wu Z Y and Xian D C 2006 *Acta Phys. Sin.* **55** 1089 (in Chinese)
[10] Wernick M N, Wirjadi O, Chapman D, Zhong Z, Galatsanos N P, Yang Y Y, Brankov J G, Oltulu O, Anastasio M A and Muehleman C 2003 *Phys. Med. Biol.* **48** 3875

[11] Oltulu O, Zhong Z, Hasnah M O, Wernick M N and Chapman D 2003 *J. Phys. D: Appl. Phys.* **36** 2152

[12] Pagot E, Cloetens P, Fiedler S, Bravin A, Coan P, Baruchel J, Härtwig J and Thomlinson W 2003 *Appl. Phys. Lett.* **82** 3421

[13] Brankov J G, Wernick M N, Yang Y Y, Li J, Muehleman C, Zhong Z and Anastasio M A 2006 *Med. Phys.* **33** 278

[14] Rigon L, Arfelli F and Menk R H 2007 *J. Phys. D: Appl. Phys.* **36** 3077

[15] Chou C Y, Anastasio M A, Brankov J G, Wernick M N, Brey E M, Connor D M and Zhong Z 2007 *Phys. Med. Biol.* **52** 1923

[16] Maksimenko A 2007 *Appl. Phys. Lett.* **90** 154106

[17] Huang Z F, Kang K J and Yang Y G 2007 *Nucl. Instrum. Method A* **579** 218

[18] Hu C H, Zhang L, Li H and Luo S Q 2008 *Opt. Express* **16** 16704

[19] Hu C H, Li H, Zhang L, Wang X Y and Luo S Q 2009 *Acta Phys. Sin.* **58** 2423 (in Chinese)

[20] Diemoz P C, Coan P, Glaser C and Bravin A 2010 *Opt. Express* **18** 3494

[21] Chen Z Q, Ding F, Huang Z F, Zhang L, Yin H X, Wang Z C and Zhu P P 2009 *Chin. Phys. C* **33** 969

[22] Muehleman C, Li J, Zhong Z, Brankov J G and Wernick M N 2006 *J. Anat.* **208** 115

[23] Hu C H, Zhao T, Zhang L, Li H, Zhao X Y and Luo S Q 2009 *Prog. Nat. Sci.* **19** 955

[24] Zhang X, Yuan Q X, Yang X R, Li H Q, Chen Y, Chen S L, Zhu P P and Huang W X 2009 *Chin. Phys. C* **33** 986

[25] Tan G, Wang H Q, Chen Y, Yuan Q X, Li G, Zhang X D, Zhu P P, Zhong X F and Tang J T 2010 *Chin. Phys. C* **34** 237

[26] Muehleman C, Fogarty D, Reinhart B, Tzvetkov T, Li J and Nesch I 2010 *Clin. Anat.* **23** 530

[27] Appel A A, Larson J C, Somo S, Zhong Z, Spicer P P, Kasper F K, Garson A B, Zysk A M, Mikos A G, Anastasio M A and Brey E M 2012 *Tissue Engineering Part. C: Method* **18** 859

[28] Appel A A, Chou C Y, Greisler H P, Larson J C, Vasireddi S, Zhong Z, Anastasio M A and Brey E M 2012 *Am. J. Surg.* **204** 631